



Rift reactivation and migration during multiphase extension



John Naliboff^{a,*}, Susanne J.H. Buitler^{a,b}

^a Geodynamics Team, Geological Survey of Norway, Trondheim, Norway

^b Centre for Earth Evolution and Dynamics, University of Oslo, Oslo, Norway

ARTICLE INFO

Article history:

Received 25 November 2014

Received in revised form 23 March 2015

Accepted 28 March 2015

Available online xxxx

Editor: Y. Ricard

Keywords:

multiphase extension

rift migration

shear zones

crustal strength

ABSTRACT

Passive margins may undergo multiple phases of extension with distinct structural, petrological and sedimentary processes before achieving breakup. Observations of rift axis migration through time may reflect cooling, hardening and subsequent abandonment of the rift axis during either long-term periods of slow extension or periods of tectonic quiescence. Here, we use 2D thermo-mechanical numerical models to examine rift reactivation and migration during multiphase extension where a period of tectonic quiescence separates phases of extension. Our goals are to identify the rheological mechanism(s) controlling rift reactivation versus migration and determine if cooling phases may help explain recent interpretations of passive margin architecture and evolution. Our numerical experiments indicate that the relative integrated brittle strength between the initial rift and surrounding regions, rather than the total integrated strength, largely controls rift reactivation versus migration. The tectonic quiescence (cooling) duration required to induce rift migration ranges between 20 and 60 Myr (minimum bounds). This range reflects variations in extension velocity, magnitude of shear zone healing, crustal rheology and asthenospheric rheology. Reactivated rifts after extensive (>20 Myr) cooling periods in some cases develop asymmetric margins with deformation patterns stepping toward the future rift, such as characterizing most of the Atlantic conjugate margins.

© 2015 Elsevier B.V. All rights reserved.

1. Introduction

Continental breakup is commonly achieved by multiple phases of lithospheric extension with distinct structural, petrological and sedimentary processes (e.g., Lister et al., 1991; Whitmarsh et al., Sep. 2001; Manatschal, 2004; Péron-Pinvidic et al., 2007, 2013; Sutra et al., 2013; Bell et al., 2014). These result in passive margins that are characterized by normal fault activity of different age and depth, deep syn- to post-rift sedimentary basins, tilted crustal blocks and possibly zones of exhumed mantle (for a review see Péron-Pinvidic et al., 2013; Franke, 2013). In addition to undergoing distinct phases of deformation, the axis of rifting can also migrate laterally through time as illustrated by the westward progression of Cenozoic rifting along portions of the Northeastern Atlantic margin (Lundin and Doré, 1997; Reemst and Cloetingh, 2000). Lateral rift migration may occur continuously through lower crustal flow and sequential faulting, leading to the formation of hyper-extended margins in the Central South Atlantic and Iberia/Newfoundland (Brune et al., 2014). In other regions of the Northeastern

Atlantic margin, however, the process of rift migration may reflect a discrete, time-dependent strengthening of the rift axis, which occurs in a period of slow extension (van Wijk and Cloetingh, 2002) or tectonic quiescence (Braun, 1992; Tett and Sawyer, 1996; Bertotti et al., 1997).

In the case of continuous and slow continental extension, conductive cooling can overcome advective heat transport within the active rift leading to cooling and thermal hardening of the lithosphere (England, 1983; Sonder and England, 1989). The combination of conductive cooling with a reduction in heat producing elements due to the active rift's crust being thinned may cause the integrated strength of the rift axis to exceed the strength of surrounding regions with thicker crust. At this stage, the original rift site can be abandoned and extension transfers to weaker regions past the rift flanks (van Wijk and Cloetingh, 2002). Similarly, separating phases of extension with a period of tectonic quiescence (i.e. multiphase) and conductive cooling may sufficiently harden the initial rift site to produce rift migration once extension resumes (Braun, 1992; Tett and Sawyer, 1996; Bertotti et al., 1997).

While these processes leading to rift migration are well established, comparatively little is known about the specific rheological mechanisms (brittle versus viscous) controlling rift migration. Here, using analytical considerations and numerical experiments, we first examine which sections of the lithosphere's strength pro-

* Corresponding author at: Geodynamics Team, Geological Survey of Norway, Leiv Eirikssons vei 39, Trondheim N-7040, Norway.

E-mail address: john.naliboff@ngu.no (J. Naliboff).

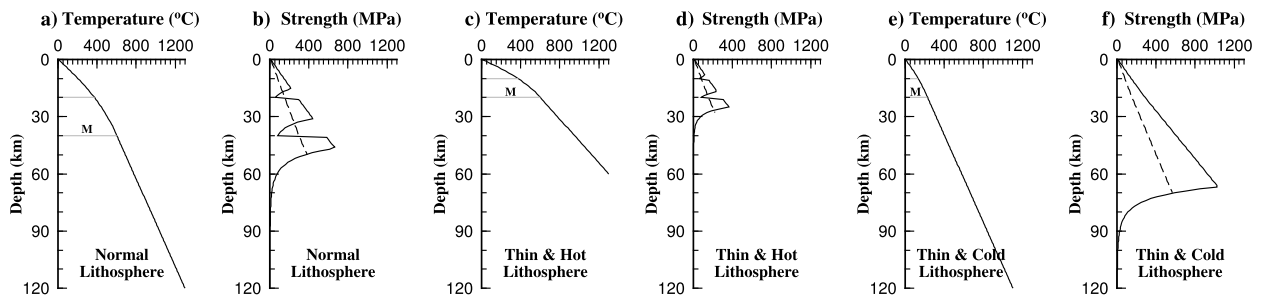


Fig. 1. Temperature and strength profiles for a 3 layer (upper and lower crust, mantle) lithosphere with a uniform extensional strain rate of $1 \times 10^{-14} \text{ s}^{-1}$. The internal angle of friction is 20 (solid line) or 10 (dashed line) degrees and the cohesion is 0 MPa. Horizontal gray lines in temperature plots (a, c, f) mark the base of the upper and lower crust. The 'M' on the lower gray line demotes Moho. a-b) Upper crust, lower crust, and lithospheric mantle thicknesses are, respectively, 20, 20, and 80 km. Temperatures at the Moho and base of the lithosphere are 602 and 1300 °C. c-d) Crust and mantle are instantaneously thinned by a factor of 2. Temperatures at the Moho and base of the lithosphere are the same as in a-b. e-f) The geotherm is determined by assuming the heat flow at the base of the lithosphere is the same as in a-b. The resulting temperatures at the Moho and base of the lithosphere, are, respectively, 229 and 578 °C. Integrated value of each strength profile in 10^{13} Pa m : 1.588 (b), 0.517 (d), 4.00 (f). Integrated value of the brittle portion of each strength profile in 10^{13} Pa m : 0.957 (b), 0.306 (d), 3.355 (f). Integrated value of the viscous portion of each strength profile in 10^{13} Pa m : 0.630 (b), 0.212 (d), 0.652 (f).

Table 1
Material densities, thermal parameters and viscous flow law parameters.

Parameter	Units	Upper cont. crust	Lower cont. crust	Lithospheric mantle	Sub-lithospheric mantle
Density (ρ_0)	kg m^{-3}	2800	2900	3250	3300
Flow law ^a	–	Wet Qtz.	Wet Anth.	Dry Olivine (disl)	Dry Olivine (diff, disl)
Visc. Prefactor (A^*) ^b	$\text{Pa}^{-n} \text{ m}^{-p} \text{ s}^{-1}$	8.57×10^{-28}	7.13×10^{-18}	6.52×10^{-16}	$2.37 \times 10^{-15}, 6.52 \times 10^{-16}$
n	–	4	3	3.5	1, 3.5
Activation energy (Q)	kJ mol^{-1}	223	345	530	375, 530
Activation volume (V)	$\text{m}^3 \text{ mol}^{-1}$	–	–	18×10^{-6}	$10 \times 10^{-6}, 18 \times 10^{-6}$
Specific heat (C_p)	$\text{J kg}^{-1} \text{ K}^{-1}$	750	750	750	750
Thermal conductivity (k)	$\text{W m}^{-1} \text{ K}^{-1}$	2.5	2.5	2.25	39.25
Thermal expansivity (α)	K^{-1}	0	0	2.5×10^{-5}	2.5×10^{-5}
T_0	°C	–	–	600	600
Heat production (H)	W m^{-3}	9×10^{-7}	9×10^{-7}	0	0
Grain size (d)	m	–	–	–	5×10^{-3}
Grain size exponent (p)	–	–	–	–	3, –

^a Flow law references: wet quartzite (Rutter and Brodie, 2004); wet anorthite (Rybacki et al., 2006); dry olivine (Hirth and Kohlstedt, 2003).

^b A^* (viscosity pre-factor) is scaled to plane strain from uniaxial strain experiments as in Ranalli (1995).

file control rift migration after a period of tectonic quiescence. Second, we explore rift migration behavior for a range of extension velocities, strength profiles, fault healing scenarios and asthenospheric rheologies. Third, we compare the characteristics of modeled reactivated and migrated rifts to recent interpretations of Atlantic continental margins. Our goal is to provide firm constraints on the physical processes controlling rift migration and place recent observations of passive margins within the context of our results.

2. Principles of rift migration

The processes of rift formation, cooling and potential migration reflect evolution of the lithosphere's strength profile (Fig. 1). We consider a lithospheric column down to 120 km depth and containing significant strength to ~50–60 km depth (Fig. 1b). The depth-dependent strength is a combination of viscous and brittle strength (see Section 3 and Table 1 for details), which largely reflects the geothermal gradient (Fig. 1a) and angle of internal friction. The geothermal gradient is determined by assigning temperatures to the surface, Moho and base of the lithosphere and then solving for the associated steady-state geotherm following (Chapman, 1986). Assigned heat production and thermal conductivity values for each layer are in Table 1.

If extension instantaneously thins the crust and mantle by a factor of 2 and preserves temperatures at the Moho and lithosphere-asthenosphere boundary (e.g., McKenzie, 1978), the resulting high, non-steady-state geothermal gradient (Fig. 1c) confines the majority of strength to above 30 km depth (Fig. 1d). Integrating the strength in Fig. 1b, d reveals that the thinned

lithosphere (Fig. 1d) has been weakened by a factor of ~3.0. Introducing a period of tectonic quiescence (no rifting) decreases the geothermal gradient due to conductive cooling and fewer total heat producing elements in the thinned crust. This leads to thermal hardening of the thinned plate.

For example, consider a cooling period that modifies temperatures such that steady-state is reached and the heat flux at the base of the crust is the same as in Fig. 1a. Temperatures at the Moho (20 km) and the base of the lithosphere (60 km) are, respectively, 229 and 578 °C (Fig. 1e). In comparison to the geotherm in Fig. 1c, these temperatures have migrated downwards by 13 or 40 km. Assuming simple 1-d time-dependent heat conduction ($t = l^2/\kappa$) (Turcotte and Schubert, 2002) and a thermal diffusivity (κ) of $1 \times 10^{-6} \text{ m}^2 \text{ s}^{-1}$, cooling over lengths (l) of 13 or 40 km requires time intervals (t) on the order of ~5–50 Myr.

Thermal hardening associated with this cooling period expands the brittle strength field (Fig. 1f) well into the asthenosphere (~60 km) and the integrated strength is now ~2.5 higher than the original lithospheric column (Fig. 1b). The ratio of the integrated strength from the brittle portions of the strength profile is even higher at ~3.5. From previous work (Braun, 1992; Tett and Sawyer, 1996; Bertotti et al., 1997; van Wijk and Cloetingh, 2002), resuming extension at this state should lead to a migration of deformation from the initial rift, which is now strong, to relatively weaker regions outside the rift. This transition and the likelihood of rift migration largely reflect the expansion of the brittle field deep into the mantle.

While this analytical assessment demonstrates the principals of rift cooling and migration, the assumption of a uniform strain-rate

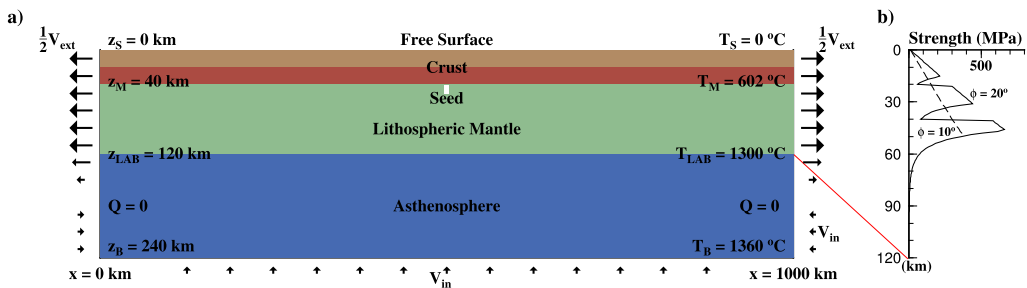


Fig. 2. a): Model dimensions, boundary conditions and lithospheric structure. b): Initial lithospheric strength profile from 0 to 120 km depth for a uniform extensional strain rate of $1\text{e-}14\text{ s}$.

throughout the lithosphere limits the applicability to specific regions. During periods of extension, the strain-rate may vary both laterally and vertically with gradients in deformation increasing as topography accumulates and deformation focuses along shear zones. In addition, variable fault weakening, rock healing and surface processes may generate significant spatial heterogeneity in strength. Accordingly, time-dependent thermo-mechanical models are required to assess the rheological mechanisms controlling the timing and style of rift migration.

3. Numerical approach

We model thermo-mechanical deformation of the lithosphere and asthenosphere using a 2-D version (3.4) of the finite element code SULEC (Ellis et al., 2011; Quinquis et al., 2011; Grigull et al., 2012; Tetreault and Buiter, 2012). SULEC solves the equations for conservation of mass (1) and momentum (2) for incompressible viscous flow:

$$\nabla \cdot u = 0 \quad (1)$$

$$\nabla \cdot \sigma' - \nabla P + \rho g = 0 \quad (2)$$

u is velocity, σ' is the deviatoric stress tensor, P is dynamic pressure, ρ is density and g is gravitational acceleration ($g_x = 0$, $g_y = -9.81\text{ m s}^{-2}$). Temperature (T) evolves through the advection-diffusion equation:

$$\rho c \left(\frac{\partial T}{\partial t} + u \cdot \nabla T \right) = \nabla \cdot k \nabla T + H \quad (3)$$

where c is specific heat, k is thermal conductivity and H is heat production. Density variations follow the Boussinesq approximation

$$\rho = \rho_0 (1 - \alpha(T - T_0)) \quad (4)$$

where α is thermal expansivity and ρ_0 is the density at the reference temperature (T_0).

Velocity and pressure are determined with an iterative penalty method (Uzawa, e.g. Pelletier et al., 1989), which transforms the momentum (Eq. (2)) and continuity (Eq. (1)) equations into

$$\nabla \cdot \sigma'^{(i)} - \nabla P^{i-1} + \nabla(K \nabla \cdot u^i) + \rho g = 0 \quad (5)$$

$$P^i = P^{i-1} - K \nabla \cdot u^i \quad (6)$$

Above, i is the pressure iteration number and K is the compressibility factor, which is 10^4 times larger than the maximum viscosity. We use Q1P0 elements, which are linear in velocity and constant in pressure.

Each 2D model maintains a geometry of 1000 km (width) by 240 km (depth) (Fig. 2), with a constant horizontal elemental resolution of 1000 m. The vertical spatial resolution is 1000 m from 0 to 120 km depth and then incrementally increases to 8000 m at 240 km depth. Materials and strain are tracked by

tracers, which initially number 9 per element but may vary between 8 and 20 during the calculation. Outward velocities (V_{ext}) on the side boundaries from 0 to 120 km depth drive extension, which is balanced by inflow (V_{in}) along the sides (180–240 km depth) and base. Horizontal velocities along the sides between 120 and 180 km linearly transition from outflow to inflow. The vertical and horizontal velocity, respectively, are unconstrained along the model sides and base, while the top boundary is a free surface. A free surface stabilization technique (Kaus et al., 2010; Quinquis et al., 2011) prevents numerical instabilities associated with numerical overshoots at density interfaces and allows for efficient time stepping. Temperature is fixed at the model base (1360°C) and surface (0°C), but unconstrained along the sides where the lateral heat flux is zero ($Q = 0$).

The model is evenly divided between continental lithosphere (0–120 km) and asthenosphere (120–240 km), with the lithosphere subdivided into upper crust (0–20 km), lower crust (20–40 km depth) and mantle (40–120 km) sections (Fig. 2). Distinct material properties distinguish each defined section (Table 1). Thermal conductivity varies between layers in accordance with an initial geotherm that is calculated using temperature and heat flux boundary conditions. We use a relatively high asthenosphere adiabat (0.5°C/km) to account for higher advective heat transport in regions with large-scale convective upwelling. High conductivity ($39.25\text{ W m}^{-1}\text{ K}^{-1}$) values in the sub-lithospheric mantle maintain this adiabatic and a constant heat flux into the lithosphere (Pysklywec and Beaumont, 2004). If the sub-lithospheric mantle cools below 1300°C , its thermal conductivity reverts to lithospheric mantle values ($2.25\text{ W m}^{-1}\text{ K}^{-1}$). For simplicity, shear heating, adiabatic heating and melting are excluded from the calculation. Material strength is defined by viscous and brittle behavior. Viscous behavior follows a power-law creep model:

$$\sigma'_{eff} = A^{-1/n} \dot{\epsilon}'_{eff}^{1/n} d^{\frac{p}{n}} e^{\frac{Q+PV}{nRT}} \quad (7)$$

σ'_{eff} is the effective stress, A is a pre-exponent, n is the power-law index, $\dot{\epsilon}'_{eff}$ is the effective strain-rate, Q is the activation energy, P is the pressure, V is the activation volume, R is the gas constant, d is the grain size and p is the grain size exponent (Table 1). The effective stress and strain-rate are defined as

$$\sigma'_{eff} = \left(\frac{1}{2} \sigma'_{ij} \sigma'_{ij} \right)^{\frac{1}{2}} \quad (8)$$

and

$$\dot{\epsilon}'_{eff} = \left(\frac{1}{2} \dot{\epsilon}'_{ij} \dot{\epsilon}'_{ij} \right)^{\frac{1}{2}} \quad (9)$$

The upper and lower crust, respectively, follow dislocation creep flow laws for wet quartzite (Rutter and Brodie, 2004) and wet anorthite (Rybacki et al., 2006). Mantle sections follow a flow law

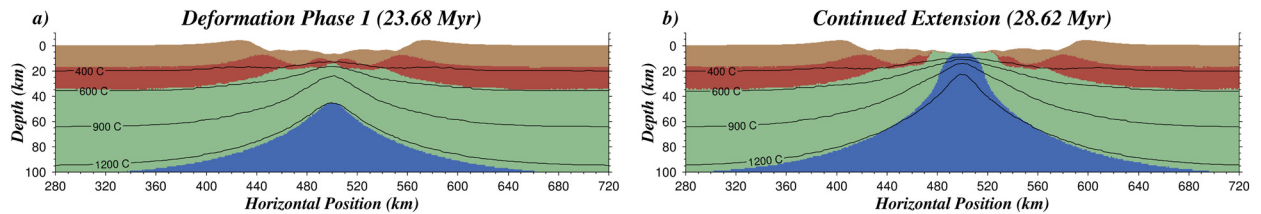


Fig. 3. Material field and thermal structure (contours in °C) after 23.68 (a) or 28.62 (b) Myr of deformation. The lithosphere extends at 1 cm yr⁻¹.

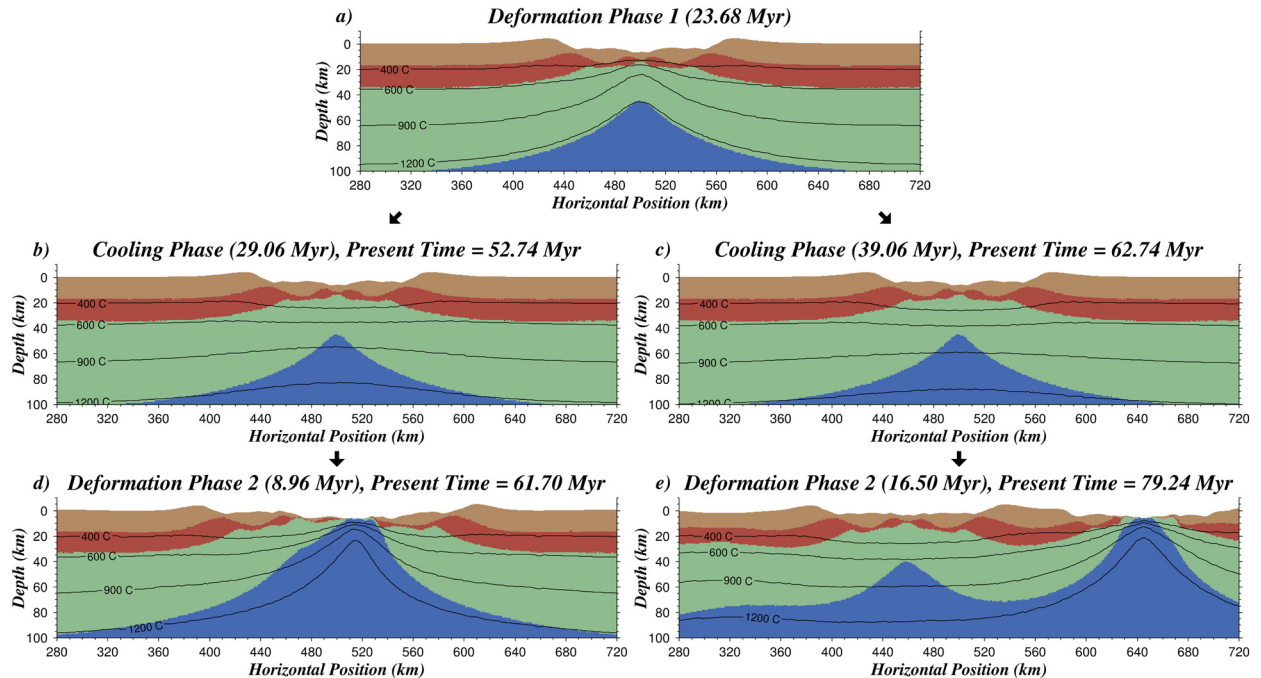


Fig. 4. Material field and thermal structure (contours in °C) after phases of deformation and cooling. During the first phase of deformation the lithosphere extends ($v_{ext} = 1 \text{ cm yr}^{-1}$) for 23.68 Myr (a). Starting from the model state after 23.68 Myr of extension, a cooling phase of ~30 (29.06) (b) or ~40 (39.06) Myr follows. Extension resumes at 1 cm yr⁻¹ in deformation phase 2, shown after 8.96 Myr (d) and 16.50 Myr (e). Rift migration occurs in the second deformation phase after ~40 Myr of cooling, while ~30 Myr of cooling leads to reactivation of the initial rift site. The viscosity field for each panel is shown in Appendix A Fig. 8.

for dry-olivine (Hirth and Kohlstedt, 2003), with the lithospheric mantle restricted to dislocation creep and the asthenosphere behaving as a composite (*comp*) between dislocation (*disl*) and diffusion (*diff*) creep (van den Berg et al., 1993):

$$\frac{1}{\eta_{comp}} = \frac{1}{\eta_{disl}} + \frac{1}{\eta_{diff}} \quad (10)$$

Viscosity is limited by minimum and maximum values of, respectively, 1e18 Pa s and 1e26 Pa s.

A Drucker-Prager yield criterion (brittle behavior) limits viscous strength according to an effective stress limit:

$$\sigma'_{eff} = Psin\phi + Ccos\phi \quad (11)$$

where ϕ is the angle of internal friction and C is cohesion (Table 1). Linear strain weakening of the friction angle (20° – 10°) and cohesion (20–10 MPa) by a factor of 2 (Bos and Spiers, 2002) between plastic strains (ϵ_p , measured by second invariant of strain tensor) of 0.5 and 1.5 promotes localization along discrete shear zones. A weak seed ($6 \times 10 \text{ km}$) with pre-weakened brittle values ($\phi = 10^\circ$, $C = 10 \text{ MPa}$) (Fig. 2) initializes deformation quickly in the crust and prevents substantial bulk shear thinning of the lithosphere in the initial phases.

The combined viscous and brittle parameters produce an initial strength profile (Fig. 2) with well defined brittle-ductile transitions

in the upper and lower crust. The strength profile evolves during two periods of deformation (weakening) and a tectonic cooling phase (hardening, separates deformation phases), with significant lateral variations in strength developing as rifting progresses. Here, we illustrate and quantify how lateral variations in the strength profile evolution during deformation and cooling phases govern rift migration.

4. Tectonic quiescence and rift evolution

We first consider a model that undergoes extension for 23.68 Myr at, $V_{ext} = 1 \text{ cm yr}^{-1}$ (Fig. 3a). Significant topographic relief and crustal thinning exists within the ~100 km wide symmetric rift zone, as well as necking of the thermal and mechanical lithosphere (Fig. 3a). An additional ~5 Myr of extension and thinning leads to full breakup of the lithosphere with predominantly symmetric conjugate margins (Fig. 3b). Starting from the lithospheric state at 23.68 Myr (Fig. 4a), the lithosphere then undergoes ~30 or ~40 Myr of tectonic quiescence ($V_{ext} = 0 \text{ cm yr}^{-1}$, Fig. 4b, c).

Lack of advective heat transport during tectonic quiescence combined with a thin crust that has less heat producing elements leads to conductive cooling and hardening of the lithosphere (Fig. 4b, c). While temperature contours after ~30 and 40 Myr of cooling reveal only slight differences, subsequent deformation

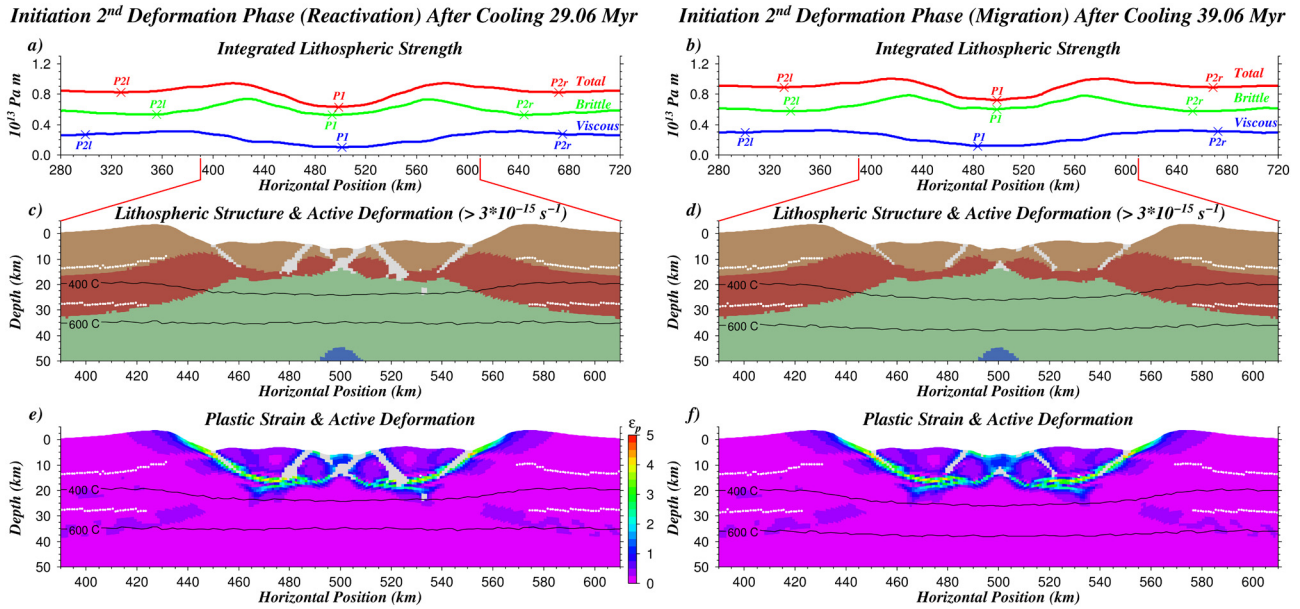


Fig. 5. Model results for 5th time step of deformation phase 2 after ~ 30 (a, c, e; Rift reactivation) or ~ 40 (b, d, f; Rift migration) Myr cooling period. Top (a, b): Integrated lithospheric strength versus horizontal position for viscous (blue), brittle (green) and brittle + viscous (red) portions of the strength profile. Curves have been smoothed (pseudo-gaussian technique) over 10 km bins. Point P1 corresponds to the minimum integrated strength value within the active rift. Points P2l and P2r, respectively, correspond to the minimum integrated strength values in the potential future rift sites. Middle (c, d): Composition, thermal structure and active deformation ($\dot{\epsilon}_{eff} > 3 \times 10^{-15} \text{ s}^{-1}$, grey regions). White dots mark the two crustal brittle-ductile transitions, which are not present through the majority of the rift site (see Fig. 1c). Bottom (e, f): Accumulated plastic strain (ϵ_p), thermal structure and active deformation. (For interpretation of the references to color in this figure legend, the reader is referred to the web version of this article.)

phases produce contrasting rifting patterns (Fig. 4d, e). In comparison to the symmetric rift developed in the first deformation phase (Fig. 3), resuming extension following ~ 30 Myr of cooling leads to asymmetric rift reactivation (Fig. 4d). In this case deformation steps outward (toward the rift center) systematically on new shear zones along the margin sides. In contrast, after ~ 40 Myr of cooling rifting migrates to a new location to the right of the original rift and dominantly symmetric deformation ensues (Fig. 4e). Notably, additional models indicate that symmetric or asymmetric deformation may develop in migrated rifts, while reactivated rifts always exhibit some degree of asymmetry.

The transition from rift reactivation to migration reflects changes in the geotherm which alter the strength contrast between the initial rift and surrounding regions. To quantify this transition, we integrate the effective stress (σ'_{eff}) from the base of the lithosphere (defined by a stress contour of 5 MPa) to the surface soon after extension resumes (5th time step). This stress field thus takes into account inherent lateral and vertical gradients in strain rate rather than assuming a fixed strain rate as in Section 2. The integrated stress, termed integrated lithospheric strength (ILS) (Fig. 5a–b, red curve), represents the lithosphere's bulk strength and thus measures the combined effects of cooling on brittle and viscous (i.e. “total”) portions of the lithosphere.

Horizontal variations in ILS after cooling ~ 30 Myr (Fig. 5a, red curve) closely follow surface topography and lithospheric structure. ILS values are low within the original rift site (low topography and thin crust), increase to maximum values at the top of rift bounding flanks and decrease to local minimum values 50–100 km past the rift flank. From this minimum, values increase to a steady value ~ 200 km from the rift center. The symbols P1, P2l, and P2r, respectively, mark minimum values inside, left and right of the rift. ILS values from brittle (Fig. 5a, green curve) or viscously (Fig. 5a, blue curve) deforming portions of the lithosphere reveal similar trends.

Cooling ~ 40 Myr (Fig. 5b) raises ILS values, albeit not systematically. The thin crust in the rift zone causes a lower thermal

gradient over this time period than after ~ 30 Myr of cooling, which is reflected in a slight downward deflection of the sub-crust isotherms (Fig. 5d). ILS trends follow a similar pattern along the rift length, although slight deviations between the two models appear within the rift axis (Fig. 5a, b). These deviations reflect 2nd phase patterns of deformation within the rift (Fig. 5c–f). Resuming extension after cooling ~ 30 Myr reactivates numerous shear zones (regions of accumulated plastic strain with low ϕ and C) within the rift (Fig. 5c, e), which progresses into large-scale rift reactivation (Fig. 4d). Fewer shear zones reactivate within the rift after ~ 40 Myr of cooling (Fig. 5d, f), which precludes rift migration (Fig. 4e).

As discussed in Section 2, in principal the transition from rift reactivation to migration should occur when the integrated strength of the plate inside the rift (point P1 on red curve, Fig. 5a, b) exceeds the minimum strength outside the rift ($\min(P2l, P2r)$ on red curve, Fig. 5a, b). At this transition the ILS ratio ($P1/\min(P2l, P2r)$) should be ~ 1 . Examination of the total (red curve) and brittle (green curve) ILS values (Fig. 5a, b) reveal, however, that the transition to rift migration occurs when the brittle ILS of the initial rift exceeds values outside the rift.

The apparent control of brittle, rather than total, ILS ratios on rift migration primarily reflects expansion of the brittle field during cooling (see Fig. 1). This expansion of the brittle fields restricts viscous deformation to the lowermost lithospheric or sub-lithospheric mantle in the original rift and places pre-existing shear zones strictly within brittle regions (Fig. 5c–f). We infer that brittle deformation outside the original rift, rather than viscous necking at the base of the plate, controls the exact location of the new rift site. The brittle deformation outside the original rift occurs within ~ 100 km wide regions in the upper crust (Appendix A Fig. 9) centered on brittle ILS minimum (Fig. 5). The location of these regions likely reflects a bending controlled transition from compressive horizontal stresses on the rift flanks to extension in the surrounding topographically low regions (Appendix A Fig. 9d). Alternatively, shear bands that reflect from the initial rift site off rheological contrasts, such as the brittle–ductile transition within

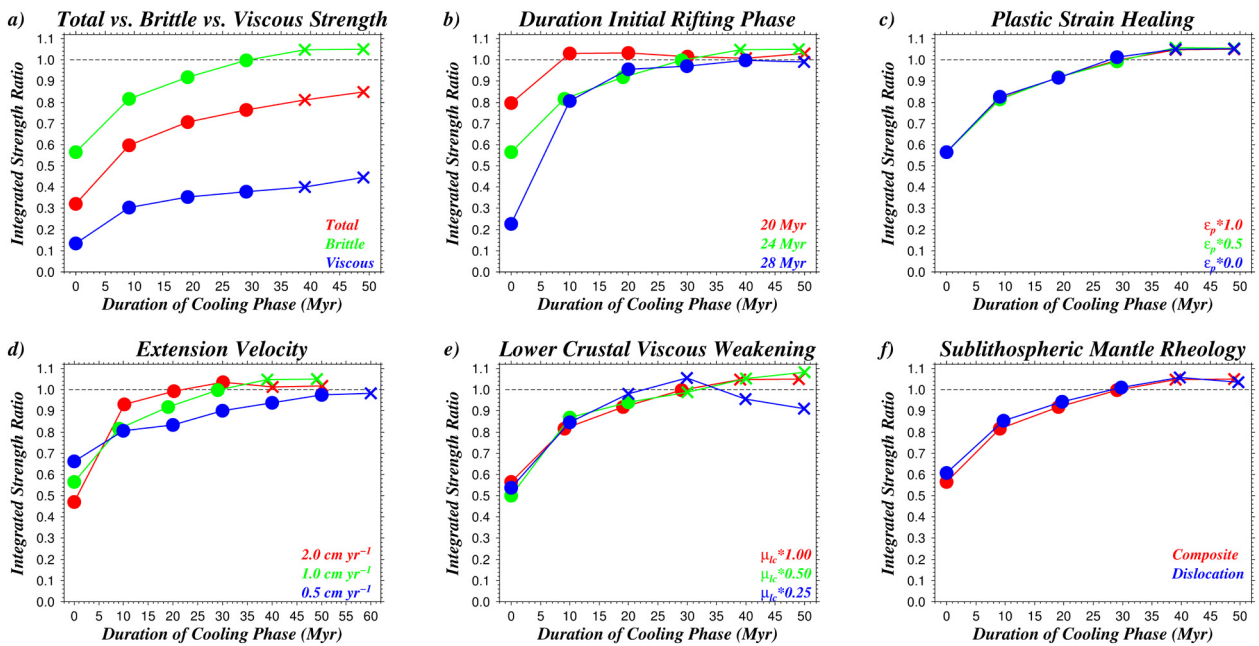


Fig. 6. Integrated lithospheric strength ratio ($ILS = P_1/\min(P_{2l}, P_{2r})$) versus the cooling phase duration (Myr). Strength ratios are calculated from the 5th time step of the second deformation phase, with the exception of points corresponding to the end of the first deformation phase (duration cooling phase = 0 Myr). Note that each point represents an individual model run. Circles and crosses, respectively, indicate rift reactivation and migration. a) Total (brittle and viscous) versus brittle versus viscous ILS ratios. Ratios in panels b-f are derived from the brittle integrated strength. b) Brittle ILS ratios for different lengths of the initial deformation phase (19.69, 23.68 or 27.84 Myr). c) Effect of removing none ($\epsilon_p * 1.0$), half ($\epsilon_p * 0.5$) or all ($\epsilon_p * 0.0$) of accumulated plastic strain after the cooling phase. d) Effect of extension velocity (2.0, 1.0 or 0.5 cm/yr) during deformation phases. e) Effect of uniformly reducing lower crustal viscosity μ_{lc} by a factor of 1 (no reduction), 2 or 4. f) Effect of asthenospheric (sub-lithospheric mantle) rheology. (For interpretation of the references to colour in this figure, the reader is referred to the web version of this article.)

the lithospheric mantle (Appendix A Fig. 9c), may focus brittle deformation in the new potential rift sites. The lack of clear reflecting shear bands connecting to the new rifting areas, however, points towards a transition in bending stresses controlling the focusing of brittle deformation outside the original rift.

Initially, brittle deformation occurs in both the new rifting areas and the initial rift zone until all deformation transfers to one of the new rift sites. The transition from deformation in multiple regions to a single new rift site is likely controlled by the non-linear nature of brittle and viscous weakening, which acts to focus deformation. Upon focusing of deformation in a single new rift site, lithospheric breakup proceeds. The 'top-down' manner of lithospheric breakup minimizes the role of viscous strength in the timing of rift migration. As a result, the ability of a rift to migrate reflects the relative strength of regions within the brittle deformation field and rift migration may occur before the total ILS strength ratio reaches 1. Analysis of ILS ratios (Fig. 6a) confirms this finding.

5. Controls on rift migration

ILS ratios for total, brittle and viscous portions of the lithosphere (Fig. 6a) systematically increase with the length of the cooling phase. This reflects increased conductive cooling within the rift compared to surrounding regions and the higher strength of mantle lithosphere replacing thinned crust within the rift. As observed in Fig. 5, the transition from rift reactivation to migration after cooling ~ 40 Myr occurs when the brittle ILS ratio is greater than 1.0 rather than the total ILS ratio.

The brittle ILS ratio at the end of the initial rift phase (cooling time = 0 Myr) reflects the duration of that period. Increasing the duration of the initial rift phase to 28 Myr (Fig. 6b) decreases the brittle ILS ratio as topographic relief, thinner crust and advective heating develop. The resulting decrease in the brittle ILS ratio (~ 0.22) increases the cooling time required for rift migration to ~ 50 Myr. For an initial deformation phase of 20 Myr, brittle ILS

ratio reach ~ 1 after ~ 10 Myr of cooling, while rift migration occurs after ~ 40 Myr of cooling. This discrepancy points toward a mechanism delaying rift migration or distinct behavior for relatively young rift systems.

Deformation in the second extension phase initially localizes in shear zones with accumulated plastic strain and weakened friction angle and cohesion values (Fig. 4c-f). In nature, shear zones may undergo strengthening (i.e. fault healing) through time (see Moresi et al., 2007 for a discussion). We simulate fault healing effects by removing half or all of accumulated plastic strain at the initiation of the second deformation phase. Fault healing minimally effects brittle ILS ratios and does not produce any change in the rift migration cooling time (Fig. 6c). This decoupling between fault healing and rift migration likely reflects that the brittle strength of pre-existing shear zones in the upper crust (upper 15 km) is small compared to the integrated strength of the expanded brittle field (>50 km depth) within the original rift. Additional experiments, however, found that removing half or all of the plastic strain could reduce the rift migration cooling time by 10 Myr. Based on this, rift migration in Fig. 6c is likely delayed between 5 and 9 Myr with the removal of plastic strain. This reduction in the cooling time required for rift migration may help explain the observed delay in rift migration for the young rift system (Fig. 6b, red curve).

Changing V_{ext} to 2.0 cm yr^{-1} has no effect on the cooling time required for rift migration (Fig. 6d). Extension rates of 1.0 and 2.0 cm yr^{-1} both require ~ 40 Myr of cooling before rift migration occurs, although brittle ILS ratios reach 1 after only ~ 20 – 30 Myr of cooling for an extension rate of 2.0 cm yr^{-1} . This delay likely partially reflects significant accumulation of plastic strain along shear zones in the original rift. Reducing the velocity to 0.5 cm yr^{-1} requires an additional 20 Myr of cooling (~ 60 Myr total) for migration to occur due to brittle ILS ratios increasing at a slower rate. This relatively slow increase of ILS ratios may reflect that

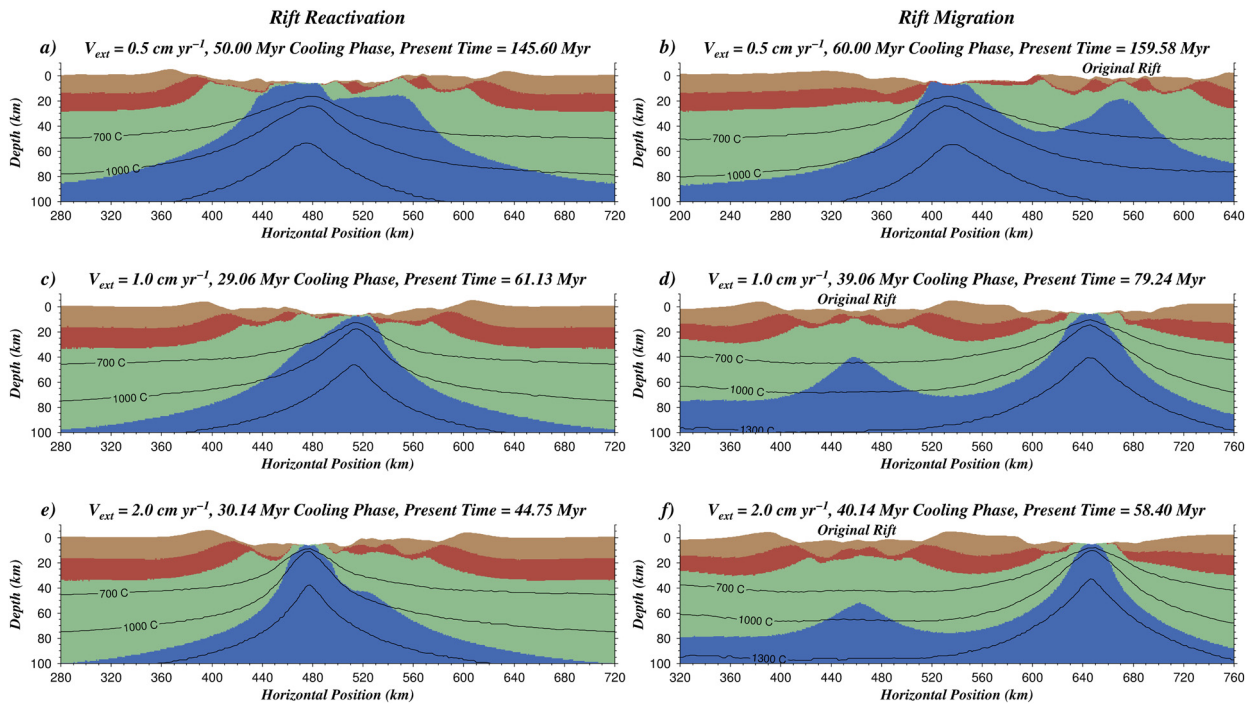


Fig. 7. Composition and thermal structure (contours in °C) during the second deformation phase. Duration of the initial rifting phase: a-b) 72.96 Myr, c-d) 23.68 Myr, e-f) 10.22 Myr. The velocity of the first and second deformation phases is the same in each model. The location of the original rift is noted in the case of rift migration.

deformation tends to focus more strongly in zones of high strain accumulation at lower background velocities.

Uniformly weakening the lower crust viscosity by a factor of 2 or 4 reduces the cooling time required for migration from ~40 Myr to, respectively, ~30 and ~20 Myr (Fig. 6e). This reduction reflects that lowering the lower crustal viscosity decreases the extent of the brittle deformation field outside of the original rift more than in the rift site with thinned crust (see Appendix A Fig. 10). Consequently, brittle ILS ratios at a given cooling time increase as the lower crustal viscosity decreases. Notably, a factor of 4 weakening generates a sharp drop in the brittle ILS ratio between cooling times of ~30 and ~50 Myr (blue curve). The decrease represents immediate focusing of brittle deformation outside the original rift site, rather than a short period of reactivation at the original rift, which significantly reduces stress magnitudes within the original rift (Appendix A Fig. 10).

Modifying the sub-lithospheric rheology to restrict it to dislocation creep (blue curve) has almost no effect on brittle ILS values and has no effect on the timing of rift migration (Fig. 6f). The viscous rheology of the sub-lithospheric mantle, however, does influence margin architecture in the case of rift reactivation and migration (Appendix A Fig. 11).

6. Comparison with observations

As a basis for comparison with observed continental margin architectures and shifting rift axes, we consider a model series of reactivated and migrated rifts for different extension velocities (Fig. 7). Rift migration and eventual breakup produces a 170–200 km separation between abandoned and new rifts (Fig. 7b, d, f). Variations in the separation distance reflect the width of the abandoned and new rifts, which also varies as a function of the initial rifting phase duration, extension velocity and lower crustal viscosity (Appendix A Fig. 10). On a first order basis, the distances between new and abandoned rifts coincide with distances between outward (away from land) stepping rift axes of ~50–100 km along the mid-Norwegian margin in Fig. 4 from Lundin and Doré (1997).

The wide (>100 km), high horst separating abandoned and migrated rifts, however, does not appear along the mid-Norwegian margin (e.g., Péron-Pinvidic et al., 2013) or Newfoundland-Iberia margins (e.g., Whitmarsh et al., Sep. 2001; Péron-Pinvidic and Manatschal, 2009; Péron-Pinvidic et al., 2013). Uplifted structures between model rifts (Fig. 7) also fail to correlate spatially or compositionally with uplifted structures (potential regions of exhumed mantle or magmatic implacement) at the end of distal domains along the mid-Norwegian margin (Møre and Vørings hights) (Reynisson et al., 2010; Péron-Pinvidic et al., 2013). However, a continental ribbon (Liverpool Land) along the mid-East Greenland margin separating an aborted inner rift basin and sag basin (Larsen, 1990; Péron-Pinvidic et al., 2013) roughly matches the width (~100 km) of modeled uplifted horsts. While the inner aborted basin is narrower than modeled abandoned rifts (Fig. 7), this could simply represent abandonment at an early stage of initial rift evolution. More likely, different initial heterogeneities, strength profiles for the crust and mantle, rift propagation and oblique extension may lead to different shear zone geometries and subsequent variations in the width of abandoned rift sections.

In comparison to crustal and mantle architectures within migrated rifts, reactivated rifts develop significant heterogeneity and asymmetry (Fig. 7a, c, e). At the beginning of the second extension phase, deformation concentrates on one side of the reactivated rift, which develops a short margin and large offset along a single normal fault. The other side of the reactivated rift develops a wider margin with a series of successive outward-stepping horst and graben structures. Qualitatively, the asymmetric distribution of material and focusing of deformation outward through time matches the first-order, outward-stepping features observed along margins in the Northern and Southern Atlantic (Whitmarsh et al., Sep. 2001; Manatschal, 2004; Péron-Pinvidic and Manatschal, 2009; Péron-Pinvidic et al., 2013). It is important to note, however, that the degree of margin asymmetry and outward stepping deformation patterns are indeed sensitive to both the extension velocity (Fig. 7) and sub-lithospheric rheology (Appendix A Fig. 11).

The required cooling times (~ 20 – 60 Myr) to induce rift migration correspond well with proposed gaps in time between three proposed rifting events (Permo-Triassic, Late Jurassic–Early Cretaceous, Late Cretaceous–Early Tertiary) along the mid-Norwegian margin (for a detailed discussion see Reemst and Cloetingh, 2000; van Wijk and Cloetingh, 2002). However, it is important to consider that new observations in these regions may reveal more continuous deformation through time without periods of significant tectonic quiescence as observed in other margins (e.g., Péron-Pinvidic et al., 2013; Sutra et al., 2013). In light of this, it is critical to consider periods of tectonic quiescence and cooling as one potential mechanism, among others (rapid strain-weakening, varying strength profiles, extension velocity) (e.g., Huismans and Beaumont, 2011; Brune et al., 2014; Tetreault and Buiter, submitted for publication), to produce patterns of deformation migration, asymmetric margins and outward stepping deformation.

7. Conclusions

Separating phases of continental extension with a period of tectonic quiescence allows conductive cooling to thermally harden the lithosphere. For sufficiently long periods of tectonic quiescence, the integrated strength of the initial rift site may surpass that of surrounding regions, leading to rift migration.

Numerical experiments of multiphase extension presented here place the required cooling time to induce rift migration between ~ 20 and 60 Myr, although testing of additional parameter space could expand this range. Analysis of the stress field at the beginning of the second extension phase reveals that the transition between rift reactivation and migration occurs when the integrated brittle strength of the rift, rather than the total integrated strength, exceeds values outside the rift. This largely reflects significant expansion of the brittle deformation field, particularly in

the original rift site, induced by cooling during periods of tectonic quiescence. Variations in extension velocity, lithospheric rheology, asthenospheric rheology or shear zone healing through time form second order controls on the cooling time required to induce rift migration.

Broadly, the cooling times required to induce rift migration match with proposed time gaps between periods of deformation along the mid-Norwegian margin. Abandoned and migrated rift structures from the numerical experiments exhibit structural similarities to an aborted rift along the mid-East Greenland margin. Some reactivated rifts that experienced extensive (>20 Myr) periods of cooling also show similar styles of outward stepping deformation and margin asymmetry as observed at Northern and Southern Atlantic passive margins. Thus, multiphase extension with periods of tectonic quiescence may help generate some of the key structural features observed at Atlantic passive margins. Future work could focus on specific regions with constraints on the magnitude and timing of deformation in order to carefully assess the role of temporally-varying velocity on passive margin architecture.

Acknowledgements

This study was supported by the Norwegian Research council through NFR project 213399/F20. SULEC is jointly developed by Susanne Buiter and Susan Ellis. All figures were made with the Generic Mapping Tools (GMT) program version 4.5 (Wessel et al., 2013). We thank Sascha Brune and Boris Kaus for insightful, thorough and highly constructive reviews. We also thank Joya Tetreault, Gwenn Péron-Pinvidic, Per Terje Osmundsen and Tim Redfield for discussions that greatly improved the manuscript.

Appendix A. Additional figures

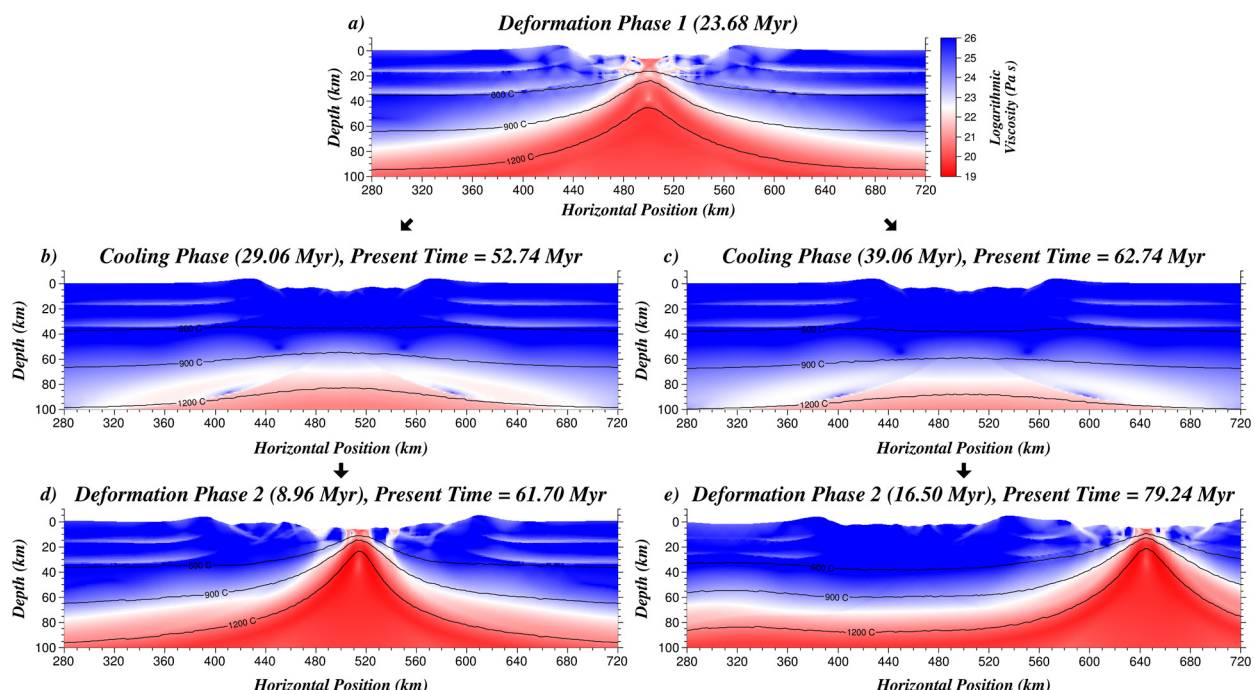


Fig. 8. Viscosity field and thermal structure (contours in $^{\circ}\text{C}$) after phases of deformation and cooling. The panels shown are equivalent to those in Fig. 4. During the first phase of deformation the lithosphere extends ($v_{\text{ext}} = 1 \text{ cm yr}^{-1}$) for 23.68 Myr (a). Starting from the model state after 23.68 Myr of extension, a cooling phase of ~ 30 (29.06) (b) or ~ 40 (39.06) Myr follows. Extension resumes at 1 cm yr^{-1} in deformation phase 2, shown after 8.96 Myr (d) and 16.50 Myr (e). Rift migration occurs in the second deformation phase after ~ 40 Myr of cooling, while ~ 30 Myr of cooling leads to reactivation of the initial rift site.

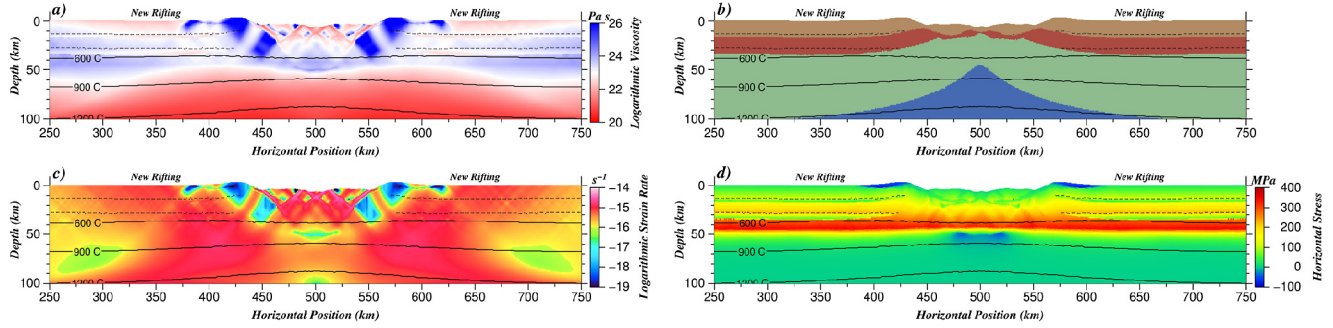


Fig. 9. Second deformation phase of the reference model undergoing rift migration (~ 40 Myr cooling time) after 5 time steps (Fig. 4a, c, e). Logarithmic viscosity (a), compositional structure (b), Logarithmic strain rate invariant (c) and horizontal stress (d) with temperature contours ($^{\circ}\text{C}$). Positive and negative horizontal stresses, respectively, represent extension and compression. Dashed lines above the temperature contours mark the two crustal brittle–ductile transitions, which are not present through the majority of the rift site. While shear zones in the initial rift are still active, 100 km wide regions in the upper crust past the rift flanks are actively deforming and weakening. The phrase *New Rifting* marks the location of these regions, which correspond to the brittle integrated strength minima in Fig. 5a–b.

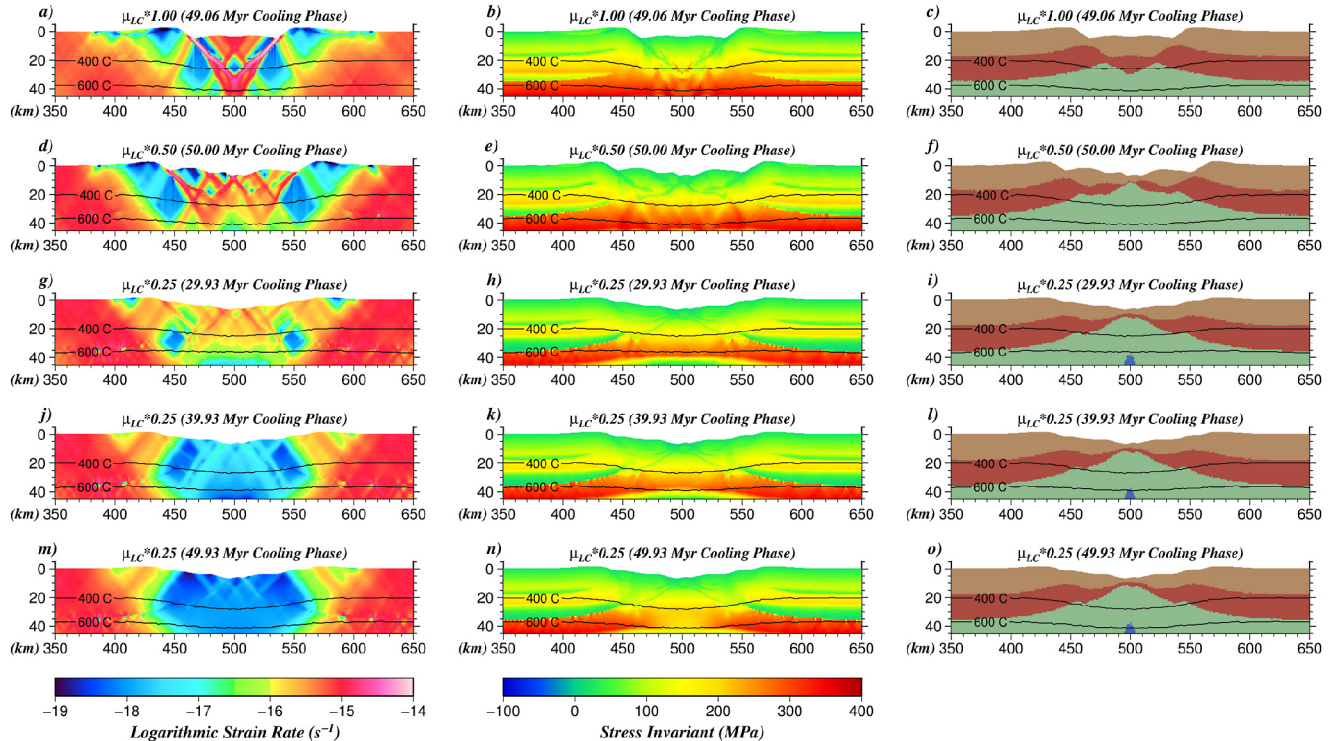


Fig. 10. Strain rate invariant, stress invariant and compositional structure with temperature contours ($^{\circ}\text{C}$) at the initiation (5th time step) of the second deformation phase for five different models. Rift migration occurs in each case. The fields are displayed for models with the reference crustal rheology (a–c), or a lower crust weakened by a factor of 2 (d–f) or 4 (g–o). The cooling times proceeding deformation are ~ 30 Myr (g–i), ~ 40 Myr (j–l) or ~ 50 Myr (a–c, d–f, m–o).

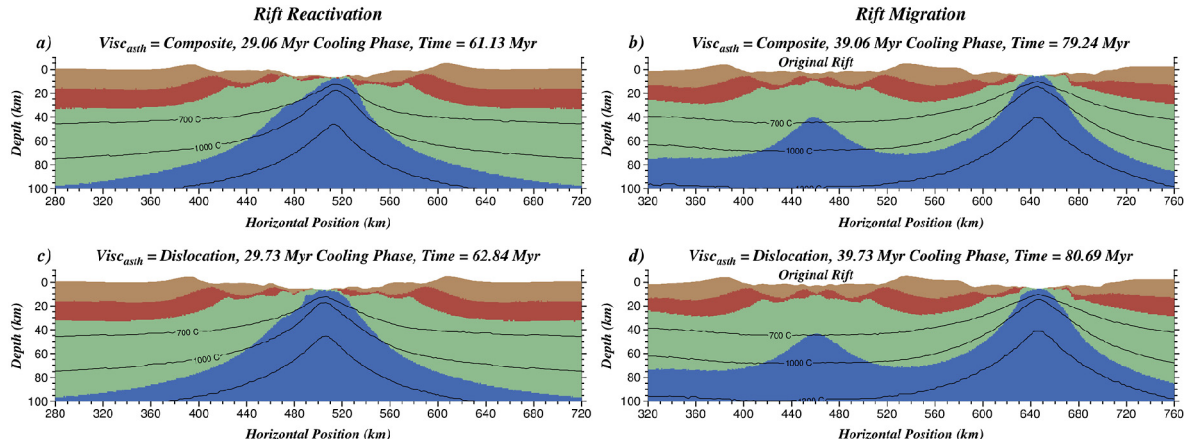


Fig. 11. Composition and thermal structure (contours in $^{\circ}\text{C}$) during the second deformation phase for distinct asthenospheric viscous rheologies (Visc_{ash}). Duration of the initial rifting phase: a–b) 23.68 Myr and c–d) 24.01 Myr. The velocity of the first and second deformation phases (1 cm/yr) is the same in each model. The location of the original rift is noted in the case of rift migration. The asthenosphere is assigned a composite (diffusion and dislocation creep) or dislocation creep dry olivine viscous flow law (Table 1).

References

- Bell, R., Jackson, C.-L., Whipp, P., Clements, B., 2014. Strain migration during multi-phase extension: observations from the northern North Sea. *Tectonics* 33 (10), 1936–1963.
- Bertotti, G., ter Voorde, M., Cloetingh, S., Picotti, V., 1997. Thermomechanical evolution of the South Alpine rifted margin (North Italy): constraints on the strength of passive continental margins. *Earth Planet. Sci. Lett.* 146 (1–2), 181–193.
- Bos, B., Spiers, C.J., 2002. Frictional-viscous flow of phyllosilicate-bearing fault rock: microphysical model and implications for crustal strength profiles. *J. Geophys. Res.* 107 (B2), 1–13.
- Braun, J., 1992. Postextensional mantle healing and episodic extension in the Canning Basin. *J. Geophys. Res., Solid Earth* 97 (B6), 8927–8936.
- Brune, S., Heine, C., Pérez-Gussinyé, M., Sobolev, S., 2014. Rift migration explains continental margin asymmetry and crustal hyper-extension. *Nat. Commun.* 5.
- Chapman, D., 1986. Thermal gradients in the continental crust. In: Dawson, J., Carswell, D., Hall, J., Wedepohl, K. (Eds.), *The Nature of the Lower Continental Crust*, vol. 24. Geol. Soc. Spec. Publ., pp. 63–70.
- Ellis, S., Little, T., Wallace, L., Hacker, B., Buitjer, S.J.H., 2011. Feedback between rifting and diapirism can exhume ultrahigh-pressure rocks. *Earth Planet. Sci. Lett.* 311 (3–4), 427–438.
- England, P., 1983. Constraints on extension of continental lithosphere. *J. Geophys. Res.* 88 (B2), 1145–1152.
- Franke, D., 2013. Rifting, lithosphere breakup and volcanism: comparison of magma-poor and volcanic rifted margins. *Mar. Pet. Geol.* 43, 63–87.
- Grigull, S., Ellis, S., Little, T., Hill, M., Buitjer, S., 2012. Rheological constraints on quartz derived from scaling relationships and numerical models of sheared brittle-ductile quartz veins, central Southern Alps, New Zealand. *J. Struct. Geol.* 37, 200–222.
- Hirth, G., Kohlstedt, D., 2003. Rheology of the upper mantle and the mantle wedge: a view from the experimentalists. In: Eiler, J. (Ed.), *Inside the Subduction Factory*. In: *Geophys. Monogr. Am. Geophys. Soc.*, vol. 138, pp. 83–105.
- Huismans, R., Beaumont, C., 2011. Depth-dependent extension, two-stage breakup and cratonic underplating at rifted margins. *Nature* 473, 74–78.
- Kaus, B.J.P., Mühlhaus, P., May, D.A., 2010. A stabilization algorithm for geodynamic numerical simulations with a free surface. *Phys. Earth Planet. Inter.* 181 (1–2), 12–20.
- Larsen, H., 1990. The East Greenland shelf. In: Grantz, A., Johnson, L., Sweeney, J. (Eds.), *The Arctic Ocean Region*. In: *The Geology of North America*. Geological Society of America, pp. 185–210.
- Lister, G.S., Etheridge, M.A., Symonds, P.A., 1991. Detachment models for the formation of passive continental margins. *Tectonics* 10 (5), 1038–1064.
- Lundin, E., Doré, A., 1997. A tectonic model for the Norwegian passive margin with implications for the NE Atlantic: early Cretaceous to break-up. *J. Geol. Soc.* 154, 545–550.
- Manatschal, G., 2004. New models for evolution of magma-poor rifted margins based on a review of data and concepts from West Iberia and the Alps. *Int. J. Earth Sci.* 93 (3), 432–466.
- McKenzie, D., 1978. Some remarks on the development of sedimentary basins. *Earth Planet. Sci. Lett.* 40, 25–32.
- Moresi, L., Mühlhaus, H.B., Lemiale, V., May, D., 2007. Incompressible viscous formulations for deformation and yielding of the lithosphere. In: Karner, G.D., Manatschal, G., Pinheiro, L.M. (Eds.), *Imaging, Mapping and Modeling Continental Lithosphere Extension and Breakup*. In: *Geol. Soc. Spec. Publ.*, vol. 282, pp. 457–472.
- Pelletier, D., Fortin, A., Camarero, R., 1989. Are fem solutions of incompressible flows really incompressible? (or how simple flows can cause headaches!). *Int. J. Numer. Methods Fluids* 9 (1), 99–112.
- Péron-Pinvidic, G., Manatschal, G., 2009. The final rifting evolution at deep magma-poor passive margins from Iberia–Newfoundland: a new point of view. *Int. J. Earth Sci.* 98, 1581–1597.
- Péron-Pinvidic, G., Manatschal, G., Minshull, T.A., Sawyer, D.S., 2007. Tectonosedimentary evolution of the deep Iberia–Newfoundland margins: evidence for a complex breakup history. *Tectonics* 26, TC2011.
- Péron-Pinvidic, G., Manatschal, G., Osmundsen, P.T., 2013. Structural comparison of archetypal Atlantic rifted margins: a review of observations and concepts. *Mar. Pet. Geol.* 43, 21–47.
- Pysklywec, R., Beaumont, C., 2004. Intraplate tectonics: feedback between radioactive thermal weakening and crustal deformation driven by mantle lithosphere instabilities. *Earth Planet. Sci. Lett.* 221, 275–292.
- Quinquis, M., Buitjer, S., Ellis, S., 2011. The role of boundary conditions in numerical models of subduction zone dynamics. *Tectonophysics* 497 (1–4), 57–70.
- Ranalli, G., 1995. *Rheology of the Earth*, 2nd edition. Chapman and Hall.
- Reemst, P., Cloetingh, S., 2000. Polypase rift evolution of the Voring margin (mid-Norway): constraints from forward tectonostratigraphic modeling. *Tectonics* 19 (2), 225–240.
- Reynisson, R., Ebbing, J., Lundin, E., Osmundsen, P.T., 2010. Properties and distribution of lower crustal bodies on the mid-Norwegian margin. In: Vining, B., Pickering, S. (Eds.), *Petroleum Geology: From Mature Basins to New Frontiers: Proceedings of the 7th Petroleum Geology Conference*. In: *Geological Society of London Petroleum Geology Conference Series*, vol. 7, pp. 843–854.
- Rutter, E., Brodie, K., 2004. Experimental grain size-sensitive flow of hot-pressed Brazilian quartz aggregates. *J. Struct. Geol.* 26, 2011–2023.
- Rybäck, E., Gottschalk, M., Wirth, R., Dresen, G., 2006. Influence of water fugacity and activation volume on the flow properties of fine-grained anorthite aggregates. *J. Geophys. Res.* 111 (B3).
- Sonder, L.J., England, P.C., 1989. Effects of a temperature-dependent rheology on large-scale continental extension. *J. Geophys. Res.* 94 (B6), 7603–7619.
- Sutra, E., Manatschal, G., Mohn, G., Unterkehr, P., 2013. Quantification and restoration of extensional deformation along the Western Iberia and Newfoundland rifted margins. *Geochem. Geophys. Geosyst.* 14 (8), 2575–2597.
- Tetreault, J.L., Buitjer, S.J.H., 2012. Geodynamic models of terrane accretion: testing the fate of island arcs, oceanic plateaus, and continental fragments in subduction zones. *J. Geophys. Res., Solid Earth* 117 (B8).
- Tetreault, J.L., Buitjer, S.J.H., submitted for publication. The influence of extension rate and crustal rheology on the evolution of passive margins from rifting to break up. *Geophys. J. Int.*
- Tett, D., Sawyer, D., 1996. Dynamic models of the multiphase continental rifting and their implications for the Newfoundland and Iberia conjugate margins. In: Whitmarsh, R., Sawyer, D., Klaus, A., Masson, D. (Eds.), *Proc. ODP, Sci. Results*. College Station, TX (Ocean Drilling Program), vol. 149, pp. 635–647.
- Turcotte, D., Schubert, G., 2002. *Geodynamics*, 2nd edition. Cambridge University Press.
- van den Berg, A., van Keken, P., Yuen, D., 1993. The effects of a composite non-newtonian and newtonian rheology on mantle convection. *Geophys. J. Int.* 115, 62–78.
- van Wijk, J.W., Cloetingh, S.A.P.L., 2002. Basin migration caused by slow lithospheric extension. *Earth Planet. Sci. Lett.* 198, 275–288.
- Wessel, P., Smith, W., Scharroo, R., Luis, J., Wobbe, F., 2013. Generic mapping tools: improved version released. *EOS Trans. AGU* 94 (45), 409–410.
- Whitmarsh, R.B., Manatschal, G., Minshull, T.A., Sep. 2001. Evolution of magma-poor continental margins from rifting to seafloor spreading. *Nature* 413 (6852), 150–154.